Photonic crystals with a degenerate band edge: Field enhancement effects and sensitivity analysis

K.-Y. Jung and F. L. Teixeira

ElectroScience Laboratory and Department of Electrical and Computer Engineering, The Ohio State University, 1320 Kinnear Road, Columbus, Ohio 43212, USA

Photonic crystals (PhCs) with a degenerate band edge (DBE) are dispersion-tailored materials composed of a periodic arrangement of misaligned anisotropic dielectric layers and an isotropic dielectric layer. DBE PhCs yield an (approximately) quartic dispersion relation just below the DBE frequency rather than the conventional quadratic dispersion relation present below a regular band edge (RBE). We present a sensitivity analysis of the performance of DBE PhCs under various perturbations. This analysis is made possible by means of an unconditionally stable finite-difference time-domain scheme to solve Maxwell's equations in anisotropic media based on a complex-envelope alternating-direction-implicit algorithm. Numerical simulations are performed to examine the gigantic field intensity enhancement at Fabry-Perot resonances associated with finite-stack DBE PhCs. Numerical simulations are also used to investigate the sensitivity of field enhancement effects against the bandwidth of the excitation. The effects of layer thickness perturbations, grounding, and dielectric losses on the electromagnetic response of DBE PhCs are also examined. The numerical results are used to compare Fabry-Perot RBE resonances against Fabry-Perot DBE resonances.

PACS number(s): 42.70.Qs, 78.20.Bh, 41.20.Jb

I. INTRODUCTION

Dispersion-engineered materials have attracted much attention for a myriad of applications at microwave, mm-wave, and optical frequency ranges. Periodic media such as photonic crystals[1–10] (PhCs) are of great interest as materials with tailored dispersion because they have simple (planar) geometries and easy frequency tunability. Magnetic photonic crystals (MPhCs) are a special class of PhCs made of misaligned anisotropic dielectric layers and ferromagnetic layers that display an asymmetric dispersion diagram $\omega(k)$ with a stationary inflection point (SIP).[3–9] MPhCs have striking electrodynamic properties such as vanishing group velocity, gigantic amplitude increase (with close to unit transmittance) at the SIP frequency, and electromagnetic unidirectionality. More recently, PhCs with a degenerate band edge (DBE) were proposed by Figotin and Vitebskiy[6,7,10] to yield a gigantic amplitude increase in nonmagnetic periodic materials. DBE PhCs can be constructed by employing, for example, two misaligned anisotropic dielectric layers and one isotropic layer in each period. DBE PhCs exhibit an approximately quartic dispersion relation just below the DBE frequency rather than the quadratic dispersion relation present below regular band edge (RBE) frequencies. In order to achieve high transmittance, Fabry-Perot resonances (associated with narrow-band transmission peaks) are exploited in finite-size periodic stacks. Finite-size DBE PhCs can produce gigantic amplitude increase at Fabry-Perot resonances with very good transmittance (matching) (Ref. 10) properties.

The detailed study of such materials—including sensitivity analysis to both geometric and material perturbations, including dielectric losses—is best done by full-wave numerical techniques, since the periodicity is broken in those cases. Among full-wave techniques for solving Maxwell's equations, the finite-difference time-domain (FDTD) method[11–13] is quite suited to simulate transient electromagnetic fields in inhomogeneous anisotropic dielectrics such as DBE PhCs.

One of the main challenges in the analysis of DBE PhCs by a finite-difference technique is that the spatial discretization cell size needs to be very small in order to correctly capture the sharp field distributions inside the structure. Unfortunately, the time step size of the conventional FDTD method is limited by the Courant stability criterion, which imposes an upper bound on the time step size based on the spatial cell size. This leads to a prohibitive number of time steps for the FDTD method. An alternative choice would be to employ the alternating-direction-implicit (ADI) FDTD algorithm,[14–17] which is an unconditionally stable method where the time step is not bound by the Courant criterion. However, the numerical accuracy of the ADI-FDTD algorithm deteriorates as the time step size and/or the maximum frequency increases.[18] Contrary to the ADI-FDTD algorithm, the numerical accuracy of the complex-envelope (CE) ADI-FDTD algorithm[19–22] is governed by the bandwidth of the excitation, not by the maximum frequency. Therefore, the CE-ADI-FDTD algorithm is especially suited for an analysis of DBE PhCs. Numerical aspects of CE-ADI-FDTD can be found elsewhere in Refs. 20 and 21.

In this work, we model the DBE PhC response in detail, examining field enhancement effects and providing a sensitivity analysis under geometric perturbations and the presence of dielectric losses. The effect of a ground plane on the DBE PhC response is also considered. The present analysis is made possible by extending the CE-ADI-FDTD algorithm to anisotropic media. The remainder of this paper is organized as follows. We first outline the basic electromagnetic properties of DBE PhCs in Sec. II. Numerical results comparing the field amplitude enhancement in DBE PhCs and RBE PhCs, as well as the effect of a ground plane on the DBE PhC response, are presented in Sec. III. In addition, a sensitivity analysis of the DBE PhC response against layer thickness variations and anisotropic dielectric losses is carried out, where a further comparison against RBE PhC is made. Concluding remarks are provided in Sec. IV. Details on the extended CE-ADI-FDTD algorithm developed here
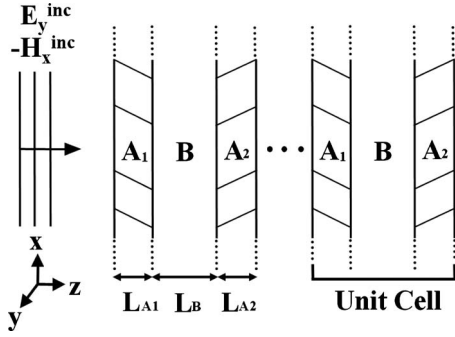
FIG. 1. Schematic of a PhC composed of two anisotropic dielectric layers (*A* layers) and one isotropic dielectric layer (*B* layer). The dispersion relation can be tailored in order to produce a degenerate band edge by adjusting the thickness and permittivity of each layer.

are included in the Appendix together with a summary of its relative computational performance.

II. DBE PHOTONIC CRYSTALS

We consider semi-infinite periodic media composed of two anisotropic layers (*A* layers) and one isotropic layer (*B* layer) depicted in Fig. 1. Here, we assume the *B* layer as air. With a proper choice of thickness and permittivity tensor parameters, one can tailor the dispersion relation to produce stationary points associated with either a RBE or DBE. As illustrated in the band diagrams shown in Fig. 2, the dispersion relation $\omega(k)$ can be approximated as $\omega_b - \omega \propto (k-k_b)^4$ just below a DBE frequency or as $\omega_b - \omega \propto (k-k_b)^2$ just below a RBE frequency, respectively, where ω_b and k_b are the angular frequency and wave number, respectively, at the band edge.[10] Below the DBE frequency, electromagnetic waves propagate at a very slow group velocity $[v_g = \partial \omega / \partial k \propto (\omega_b - \omega)^{3/4}]$.

In the infinite-medium case, the transmittance decreases and gradually approaches zero as the frequency ω ap-
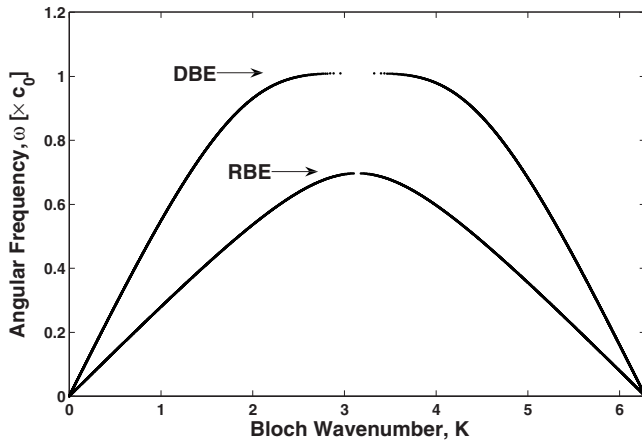

FIG. 2. Band diagram showing both a DBE and a RBE. The dispersion relation can be approximated by a quartic polynomial just below the DBE frequency and by a quadratic polynomial just below the RBE frequency (see text for details).
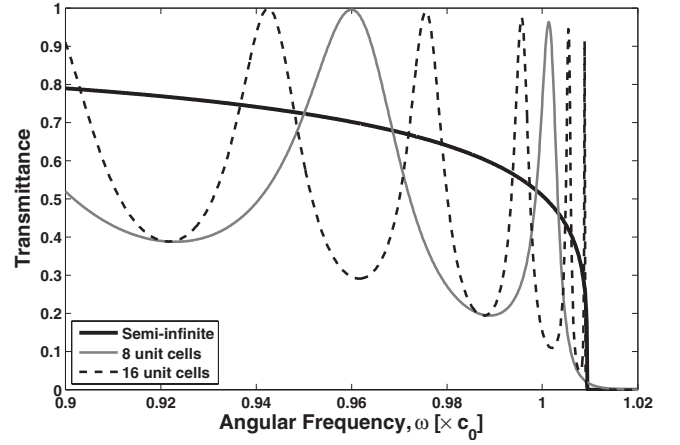

FIG. 3. Transmission spectrum of finite-stack DBE PhCs. Larger *N* leads to Fabry-Perot resonance frequencies closer to the band edge and to narrower transmission bands.

proaches either the DBE or RBE from below. However, when a truncated (finite number of stacks) DBE PhC is considered, Fabry-Perot cavity resonances are produced depending on the number *N* of unit cells. The resonances below the DBE frequency are shown for $N=8$ and $N=16$ in Fig. 3. As *N* increases, the Fabry-Perot resonance frequencies move close to the DBE frequency (while the transmission bands are narrowed). As Fabry-Perot resonances move just below the band edge, a dramatic increase in field intensity is produced because of the wave slowdown (decrease in the group velocity), similar to what occurs in MPhCs.[4] Hence, a larger *N* leads to greater growth in field intensity. We also mention here that because the group velocity is smaller below the DBE frequency (from the quartic dispersion relation) than the RBE frequency (from the quadratic dispersion relation), a much larger increase in the field amplitude is produced at DBE-based Fabry-Perot resonances than at the RBE counterpart (for same *N*).

III. METHOD OF ANALYSIS

We next examine the PhCs considered in Ref. 10 using the CE-ADI-FDTD algorithm described in the Appendix. To validate the present CE-ADI-FDTD algorithm, CE-ADI-FDTD results are compared with FDTD results, showing very good agreement (see the Appendix). The accuracy of CE-ADI-FDTD results is nearly invariant unless the time-step Δt is made close to the Nyquist limit.[23] Therefore, computational time can be greatly reduced utilizing CE-ADI-FDTD simulations, since one can choose a much larger Δt for a given accuracy versus the conventional FDTD method. This makes it practical to carry out the sensitivity analysis presented in this paper.

The constitutive tensor (relative) parameters are $\epsilon_{A1} = \epsilon_{A2} = 13.61$, $\delta_{A1} = \delta_{A2} = 12.4$, $\varphi_{A1} = 0°$, $\varphi_{A2} = 45°$, and $\mu_{r,A1} = \mu_{r,A2} = 1$ [see Eq. (A10)], as considered in Ref. 10. The excitation is a raised-cosine-ramped sine wave with unit peak amplitude whose carrier angular frequency ω_c corresponds to the first Fabry-Perot resonance. The layer thick-
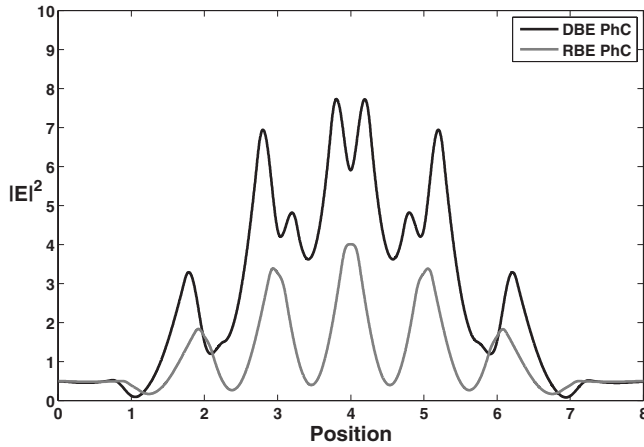
FIG. 4. Steady-state time-averaged field intensity $|\mathbf{E}|^2$ inside a PhC with $N=8$. The incident wave has unit amplitude. Further increase in the field intensity is observed in the DBE PhC versus the RBE PhC.

nesses are as follows: $L_{A1}=L_{A2}=0.270\,545$ m and L_B $=0.458\,91$ m for DBE PhCs and $L_{A1}=L_{A2}=0.120\,545$ m and $L_B=0.758\,91$ m for RBE PhCs. This choice yields the angular frequency of the first resonance near c_0 rad/s for DBE PhCs and $1.6c_0$ rad/s for RBE PhCs, respectively, where c_0 is the numerical value of vacuum light speed in m/s. The space step is $\Delta z=1/400$ m, multiplied by different κ factors inside each layer to match the respective thicknesses. We choose $\kappa_{A1}=\kappa_{A2}=0.270\,545/0.27$ and κ_B $=0.458\,91/0.46$ for the DBE PhC simulations here. The time step size is given by $\Delta t=N_C\kappa_B\Delta z/c_0$, where N_C is the Courant number (CN). A Courant number $N_C=250$ is used unless specified otherwise.

IV. INTENSITY ENHANCEMENT RESULTS

First, we analyze a DBE PhC with $N=8$. Figure 4 shows the steady-state time-averaged field intensity ($|\mathbf{E}|^2$) inside this finite-stack DBE PhC. The incident field has unit amplitude. Note that the field distribution has sharp variations inside the DBE PhC, which illustrates the need for a very fine mesh resolution. For comparison, we also show the results for a RBE PhC with $N=8$. The field intensity in the DBE PhC is about twice that of the RBE PhC.

Figure 5 shows the steady-state time-averaged $|\mathbf{E}|^2$ inside the DBE PhC with $N=16$ and inside the RBE PhC with N $=16$. As illustrated in Fig. 3, the resonance bandwidth in this case is narrower than with $N=8$, but the resonance closer to the band edge. The gigantic enhancement in the field intensity inside the DBE PhC is clearly visible, with the field intensity ratio of the DBE PhC to the RBE PhC being about 5.

We next consider the analysis of a DBE PhC with N $=32$. From convergence tests, it is determined that simulations with $\Delta z=1/400$ m cannot accurately analyze a DBE PhC that long. In this case, $\Delta z=1/1600$ m is required to capture even sharper field distributions. To make the matter worse, longer time integration times should be employed to
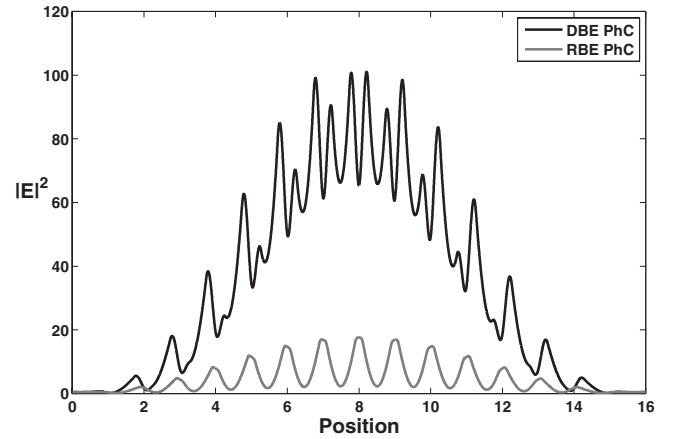
obtain the necessary frequency resolution given the narrower Fabry-Perot resonance with $N=32$. Those two requirements—very small Δz and long integration times— make it very challenging to simulate DBE PhCs with N $=32$. We mention that it would not be practical to simulate this DBE PhC by either the conventional FDTD or ADI-FDTD algorithm under our available computing resources. For analysis of the DBE PhC with $N=32$, the CE-ADI-FDTD algorithm with $N_C=500$ is employed. Figure 6 shows the steady-state time-averaged $|\mathbf{E}|^2$ inside the DBE PhC with $N=32$ and inside the RBE PhC with $N=32$, illustrating the great difference in the intensity increase. A curve fit for these examples indicates that the peak field intensity is proportional to about $N^{3.8}$ for DBE PhCs and $N^{1.9}$ for RBE PhCs.

Next, we employ a sine-wave-modulated Gaussian pulse to illustrate the impact of the fractional bandwidth on field enhancement effects. In this case, $N_C=50$ is employed. Fig-
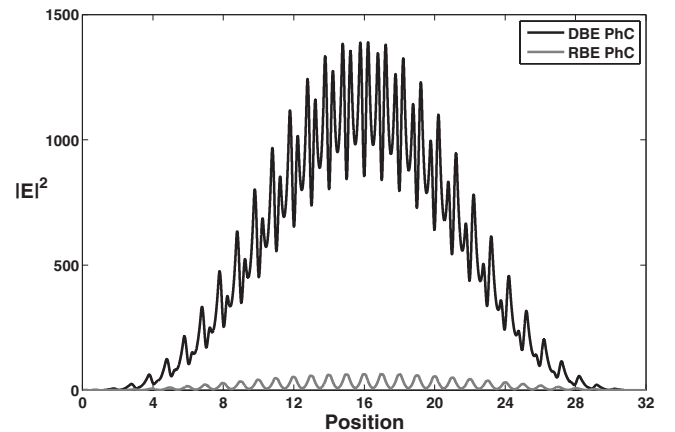

FIG. 5. Steady-state time-averaged field intensity $|\mathbf{E}|^2$ inside a PhC with $N=16$. The incident wave has unit amplitude. Further increase in the field intensity is observed in the DBE PhC versus the RBE PhC.

FIG. 6. Steady-state time-averaged field intensity $|\mathbf{E}|^2$ inside a PhC with $N=32$. The incident wave has unit amplitude. A much larger field intensity is observed in the DBE PhC versus the RBE PhC. Note the larger difference between the relative intensities versus Figs. 4 and 5.
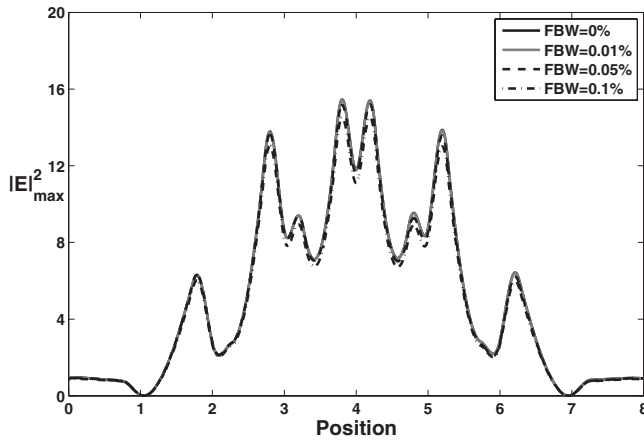
FIG. 7. Maximum field intensity $|\mathbf{E}|^2_{max}$ inside the DBE PhC with $N=8$ under sine-wave-modulated Gaussian pulse excitations. Large fractional bandwidth (FBW) leads to a decrease on field enhancement effects. Here, FBW=0% means a sine-wave excitation (without Gaussian pulse modulation).

ure 7 and Fig. 8 show the maximum field intensity $|\mathbf{E}|^2_{max}$ inside the DBE PhC with $N=8$ and inside the DBE PhC with $N=16$, respectively. As the fractional bandwidth increases, the enhancement in the field intensity decreases. A narrower transmittance bandwidth of the Fabry-Perot resonance for $N=16$ versus $N=8$ leads to a greater impact of the fractional bandwidth on field enhancement effects (see Fig. 3).

V. SENSITIVITY ANALYSIS

A. Ground plane effects

In what follows, the time-domain excitation is a raised-cosine-ramped sine wave. Next, we illustrate ground plane effects on the DBE PhC response. The ground plane is on the far end of the DBE PhC. We assume the ground plane to be a perfect electric conductor (PEC). Figure 9 shows the steady-state time-averaged $|\mathbf{E}|^2$ inside the PEC-backed DBE PhC with $N=8$, showing an approximately fivefold increase
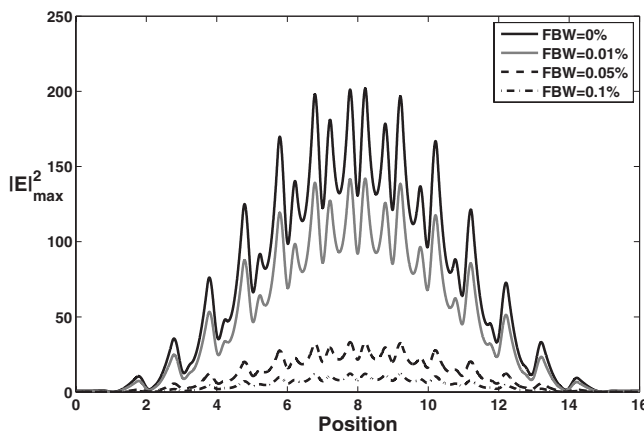

FIG. 8. Same as Fig. 7 for the DBE PhC with $N=16$. The effect of the FBW on the field intensity is more pronounced for the $N=16$ case, compared to the $N=8$ case.

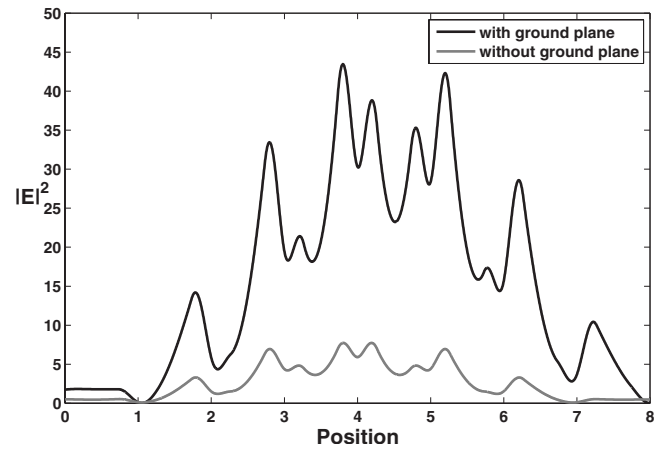

FIG. 9. Ground plane effect on the response of the DBE PhC with $N=8$. The relative increase in the field intensity due to the ground plane is about fivefold. Note that the field distribution becomes asymmetric.

in the field intensity compared to the case with no ground plane. We note that the spatial distributions in field intensity are not symmetric anymore. We also examine the effects of the ground plane on the DBE PhC with $N=16$ and $N=32$. A similar increase of the field intensity and nonsymmetric field intensity distributions results from including a ground plane, as shown in Figs. 10 and 11. The peak intensity increase due to the ground plane is 5.63, 4.03, and 4.04 for $N=8$, $N=16$, and $N=32$, respectively. The increase in the field intensity can be attributed to (higher) resonance frequencies closer to the DBE frequency, thus having slower group velocity.

B. Layer thickness perturbations

Next, we assess the sensitivity of PhC responses to layer thickness perturbations. For this purpose, we randomly perturb the thickness of all cells for the PhC with $N=16$. The thickness of each cell is assumed to be a (independent)
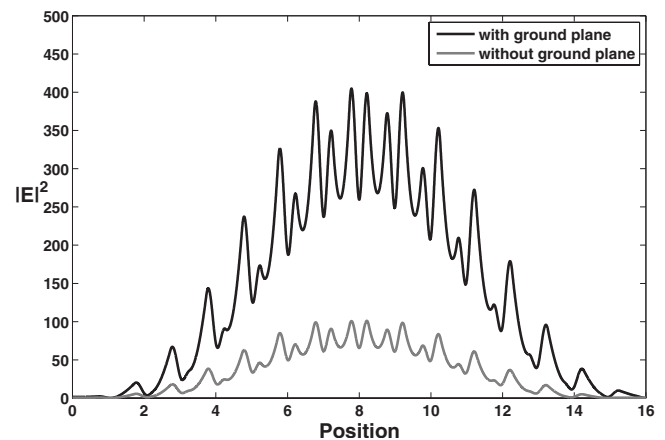

FIG. 10. Ground plane effect on the response of the DBE PhC with $N=16$. The relative increase in the field intensity due to the ground plane is about fourfold. Note that the field distribution becomes slightly asymmetric.
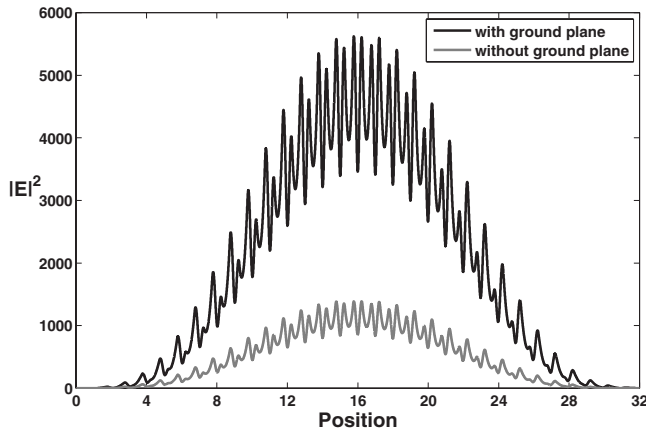
FIG. 11. Ground plane effect on the response of the DBE PhC with $N=32$. The relative increase in the field intensity due to the ground plane is again about fourfold.

Gaussian random variable centered on the nominal thickness. For each variance, an ensemble with 12 realizations is considered. Figure 12 shows the steady-state time-averaged $|\mathbf{E}|^2$ inside the DBE PhC with the perturbed layer thickness. As can be seen from this figure, small variations in the layer thickness can have a strong impact on the DBE PhC performance (due to the sensitivity of the Fabry-Perot resonance to geometrical parameters). Figure 13 shows the steady-state time-averaged $|\mathbf{E}|^2$ inside the RBE PhC with the same thickness perturbations. It is observed that the RBE PhC is less sensitive to the layer thickness perturbations compared to the DBE PhC. Figure 14 displays the peak value of $|\mathbf{E}|^2$ inside the DBE PhC and RBE PhC under various layer thickness perturbations and PhC sizes. The DBE PhC with $N=16$ produces less enhancement in the field intensity than the RBE PhC with $N=16$ when the layer thickness is perturbed by about 0.3%. We also display the peak value of $|\mathbf{E}|^2$ inside the RBE PhC with $N=38$ (which has a similar performance in terms of intensity increase to the DBE PhC with $N=16$). As shown in Fig. 14, the DBE PhC with $N=16$ is similarly sensitive to the considered layer thickness perturbations as
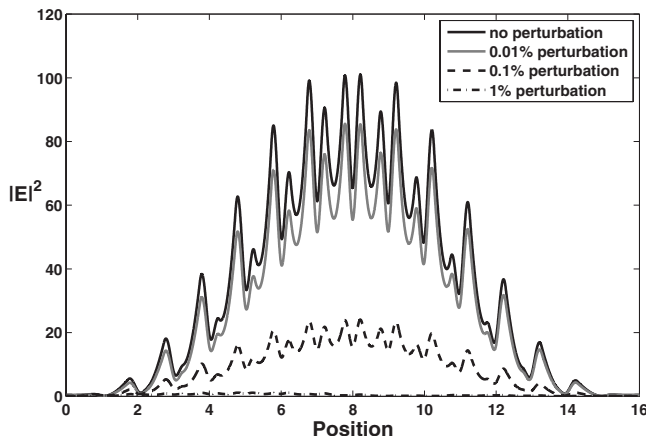

FIG. 12. Effect of layer thickness perturbations on the response of the DBE PhC with $N=16$. Small thickness perturbations lead to a decrease on field enhancement effects, as expected.
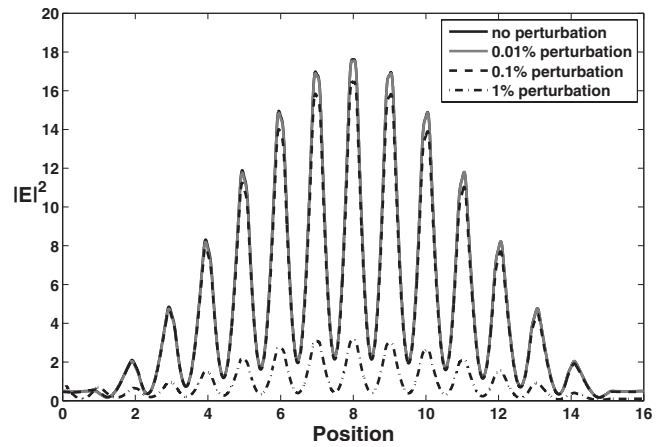

FIG. 13. Effect of layer thickness perturbations on the response of the RBE PhC with $N=16$. The decrease is relatively less pronounced than for the DBE PhC with $N=16$, but the absolute intensity enhancements are still well below those produced by the DBE PhC under 0.1% perturbations; see Fig. 12.

the RBE PhC with $N=38$, with the former yielding a little bit smaller field intensity. Table I summarizes the peak value of field intensity under considered layer thickness perturbations.

C. Dielectric losses

The sensitivity of the PhC response to dielectric losses in the A layers is illustrated in Fig. 15, where a loss tangent of 10^{-4} produces a 60% decrease in the peak field intensity in the DBE PhC and a 10% decrease in the peak field intensity in the RBE PhC for the same number of $N=16$ layers. Note how the DBE PhC with $N=16$ shows a very similar sensitivity curve as the RBE PhC with $N=38$. It should be further noted that dielectric losses change the resonance peak frequency somewhat, as shown in Fig. 16. Therefore, the results presented in Fig. 15 also include any detuning effect in the
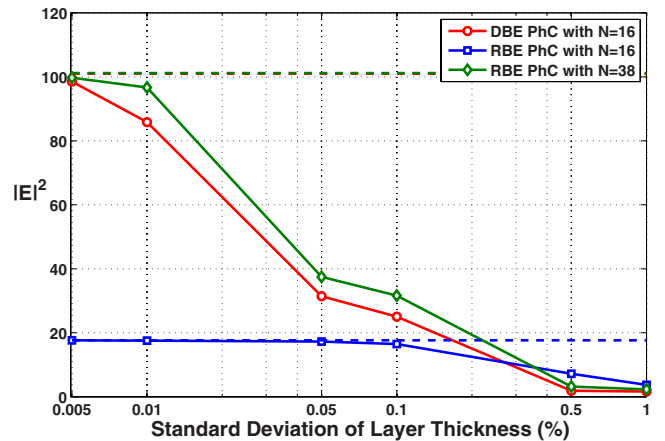

FIG. 14. (Color online) Peak value of $|\mathbf{E}|^2$ inside PhCs with layer thickness perturbations. The thickness of each cell is randomly perturbed. For each standard deviation, 12 realizations are produced and the average results for each standard deviation are plotted. The dashed lines indicate nonperturbed PhC results.

TABLE I. Field intensity under layer thickness perturbations.

Perturbations	DBE ($N=16$)	RBE ($N=16$)	RBE ($N=38$)
0.005%	98.5167	17.6172	99.7660
0.01%	85.8719	17.5628	96.7120
0.05%	31.4252	17.2379	37.4918
0.1%	25.0403	16.4865	31.6033
0.5%	1.8743	7.1981	3.1802
1%	1.6433	3.7178	2.3190

Fabry-Perot resonances produced by the dielectric losses, since the frequency of the excitation signal is kept constant.

VI. SUMMARY AND CONCLUSION

We examined Fabry-Perot resonances in finite-stack DBE PhCs. The gigantic amplitude increase produced by such resonances was contrasted to similar effects yielded by RBE PhCs. The numerical analysis has shown that the field intensity inside DBE PhCs increases approximately as $N^{3.8}$, where N is the number of unit cells. It has been observed that a ground plane can boost the field intensity inside DBE PhCs. In particular, the peak field intensity inside DBE PhCs with $N=8$ and $N=16$, and backed by ground planes, is about 5.6 and 4 times larger, respectively, than the peak field intensity inside DBE PhCs with equal lengths.

We have performed a sensitivity analysis of DBE PhC responses under perturbations on geometrical (layer thickness) and material (dielectric losses) parameters and compared the impact of these perturbations on the DBE and RBE PhC responses. As expected, the field intensity enhancement in DBE PhCs deteriorates under small perturbations of the layer thickness. On the other hand, the overall response is quite robust to the presence of dielectric losses. For the DBE
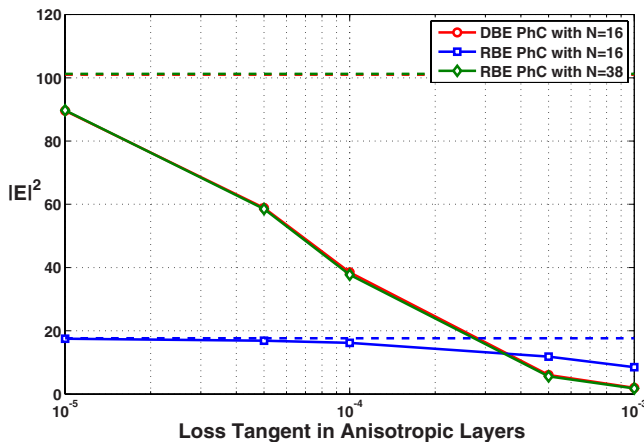

FIG. 15. (Color online) Peak value of $|\mathbf{E}|^2$ inside PhCs with losses in A layers. The dashed lines indicate lossless PhC results. For the same N, the DBE PhC is more sensitive to dielectric losses than the RBE PhC. However, considering similar (field enhancement) performance, the DBE PhC with $N=16$ shows similar sensitivity to the considered dielectric losses as the RBE PhC with $N=38$.
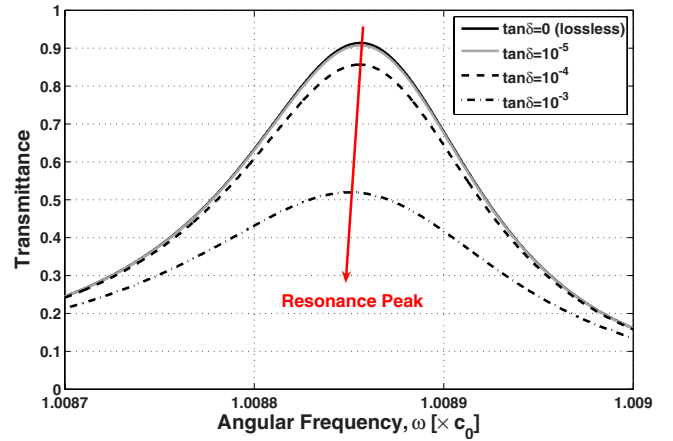

FIG. 16. (Color online) Effect of dielectric losses on the first Fabry-Perot resonance of the DBE PhC with $N=16$. The resonance peak frequency is slightly shifted to lower frequencies by the dielectric losses.

PhC with $N=16$, a loss tangent of 10^{-5} decrease the peak intensity by only about 10%.

A full-wave CE-ADI-FDTD algorithm has been developed to anisotropic media based on a **D**-**H**-**E** formulation to decouple the update of the constitutive equations from the update of the Maxwell's curl equations written in terms of (complex) field envelopes. The CE-ADI-FDTD algorithm is advantageous over both conventional FDTD and ADI-FDTD algorithms for DBE PhC analysis, with a dramatic reduction on the overall computation time being achieved. Contrary to the traditional ADI-FDTD algorithm, the numerical dispersion error of the CE-ADI-FDTD algorithm for narrow-band problems remains small unless the time step size approaches the Nyquist limit.

APPENDIX: CE-ADI-FDTD ALGORITHM FOR ANISOTROPIC MEDIA

In this appendix, we describe the CE-ADI-FDTD algorithm used in the analysis.

Consider an anisotropic media with anisotropy in the xy plane under a y-polarized plane wave propagating along z, as illustrated in Fig. 1. Both x and y components should be considered simultaneously due to the cross coupling of transverse electric and magnetic components. Maxwell's curl equations are expressed as

$$\frac{\partial}{\partial t}D_x + \frac{\sigma_z}{\epsilon_0}D_x = -\frac{\partial}{\partial z}H_y, \qquad (A1)$$

$$\frac{\partial}{\partial t}D_y + \frac{\sigma_z}{\epsilon_0}D_y = \frac{\partial}{\partial z}H_x, \tag{A2}$$

$$\frac{\partial}{\partial t}H_x + \frac{\sigma_z}{\epsilon_0}H_x = \frac{\partial}{\mu\,\partial z}E_y, \tag{A3}$$

$$\frac{\partial}{\partial t}H_y + \frac{\sigma_z}{\epsilon_0}H_y = -\frac{\partial}{\mu\,\partial z}E_x. \tag{A4}$$

In the above, σ_z is the *artificial* conductivity profile along the z direction that implements a perfectly matched layer absorbing boundary condition.[24–27] Conventional Maxwell's curl equations are recovered by setting $\sigma_z = 0$.

We assume $\mathbf{F} = \mathrm{Re}[\widetilde{\mathbf{F}}\cdot e^{j\omega_c t}]$, where ω_c is the carrier frequency, $\mathbf{F}$ denotes the field components, and $\widetilde{\mathbf{F}}$ denotes the corresponding complex envelope. Maxwell's curl equations in terms of the complex envelopes are expressed as

$$\frac{\partial}{\partial t}\widetilde{D_x} + j\omega_c\widetilde{D_x} + \frac{\sigma_z}{\epsilon_0}\widetilde{D_x} = -\frac{\partial}{\partial z}\widetilde{H_y}, \tag{A5}$$

$$\frac{\partial}{\partial t}\widetilde{D_y} + j\omega_c\widetilde{D_y} + \frac{\sigma_z}{\epsilon_0}\widetilde{D_y} = \frac{\partial}{\partial z}\widetilde{H_x}, \tag{A6}$$

$$\frac{\partial}{\partial t}\widetilde{H_x} + j\omega_c\widetilde{H_x} + \frac{\sigma_z}{\epsilon_0}\widetilde{H_x} = \frac{\partial}{\mu\,\partial z}\widetilde{E_y}, \tag{A7}$$

$$\frac{\partial}{\partial t}\widetilde{H_y} + j\omega_c\widetilde{H_y} + \frac{\sigma_z}{\epsilon_0}\widetilde{H_y} = -\frac{\partial}{\mu\,\partial z}\widetilde{E_x}. \tag{A8}$$

The relevant constitutive equation is written as

$$\widetilde{\mathbf{D}} = [\epsilon]\widetilde{\mathbf{E}}, \tag{A9}$$

with permittivity tensor of the form

$$[\epsilon] = \epsilon_0 \begin{bmatrix} \epsilon_{xx} & \epsilon_{xy} & 0 \\ \epsilon_{xy} & \epsilon_{yy} & 0 \\ 0 & 0 & \epsilon_{zz} \end{bmatrix}$$

$$= \epsilon_0 \begin{bmatrix} \epsilon + \delta\cos(2\varphi) & \delta\sin(2\varphi) & 0 \\ \delta\sin(2\varphi) & \epsilon - \delta\cos(2\varphi) & 0 \\ 0 & 0 & \epsilon_{zz} \end{bmatrix}, \tag{A10}$$

where the parameter δ is the magnitude of the in-plane anisotropy and φ is the orientation angle of the principal axis of the permittivity tensor in the xy plane.

In the ADI algorithm,[14,15] the update at each time step n is divided into two substeps. For simplicity, we omit the tilde in update equations that follow. For the first substep, discretized equations from Maxwell's curl, Eqs. (A5)–(A8), can be written as

$$D_{x_k}^{n+1/2} = c_{d1}D_{x_k}^n - c_{d2}[H_{y_{k+1/2}}^n - H_{y_{k-1/2}}^n], \tag{A11}$$

$$D_{y_k}^{n+1/2} = c_{d1}D_{y_k}^n + c_{d2}[H_{x_{k+1/2}}^{n+1/2} - H_{x_{k-1/2}}^{n+1/2}], \tag{A12}$$

$$H_{x_{k+1/2}}^{n+1/2} = c_{h1}H_{x_{k+1/2}}^n + c_{h2}[E_{y_{k+1}}^{n+1/2} - E_{y_k}^{n+1/2}], \tag{A13}$$
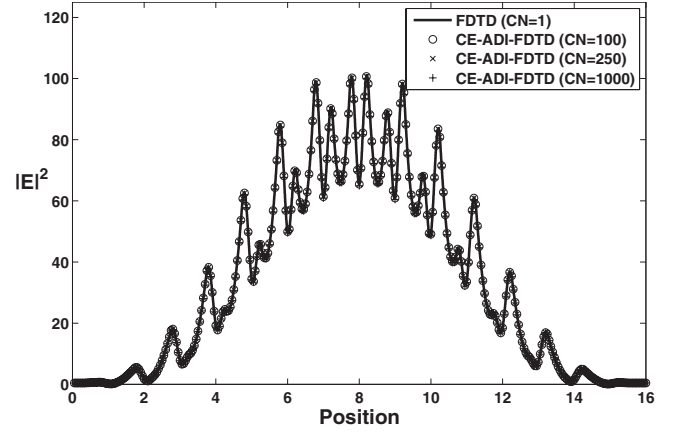

FIG. 17. CE-ADI-FDTD results using various CNs for the steady-state time-averaged field intensity $|\mathbf{E}|^2$ inside the DBE PhC with $N=16$.

$$H_{y_{k+1/2}}^{n+1/2} = c_{h1}H_{y_{k+1/2}}^n - c_{h2}[E_{x_{k+1}}^n - E_{y_k}^n], \tag{A14}$$

where the subscript refers to spatial grid indexing along z and the superscript refers to the time step index. The coefficients above are given by $c_{d1} = c_{h1} = \alpha_-/\alpha_+$ and $c_{d2} = \mu c_{h2} = \alpha_0/\alpha_+$, where $\alpha_\pm = 1 \pm 0.25\Delta t(j\omega_c + \sigma_z/\epsilon_0)$ and $\alpha_0 = 0.5\Delta t/\Delta z$. The update equation for $\widetilde{E}$ can be obtained from the constitutive equation (A9) as

$$E_{x_k}^{n+1/2} = c_{e1x}D_{x_k}^{n+1/2} + c_{e2}D_{y_k}^{n+1/2}, \tag{A15}$$

$$E_{y_k}^{n+1/2} = c_{e1y}D_{y_k}^{n+1/2} + c_{e2}D_{x_k}^{n+1/2}, \tag{A16}$$

where $c_{e1x} = \epsilon_{yy}/(\epsilon_0\Lambda_e)$, $c_{e1y} = \epsilon_{xx}/(\epsilon_0\Lambda_e)$, and $c_{e2} = -\epsilon_{xy}/(\epsilon_0\Lambda_e)$, with $\Lambda_e = \epsilon_{xx}\epsilon_{yy} - \epsilon_{xy}^2$. From Eq. (A12), we see that $D_y^{n+1/2}$ cannot be updated explicitly. By substituting Eq. (A16) into Eq. (A13) and plugging the resulting equation into Eq. (A12), we obtain an implicit equation for $D_y^{n+1/2}$ in a form of the tridiagonal system as follows:
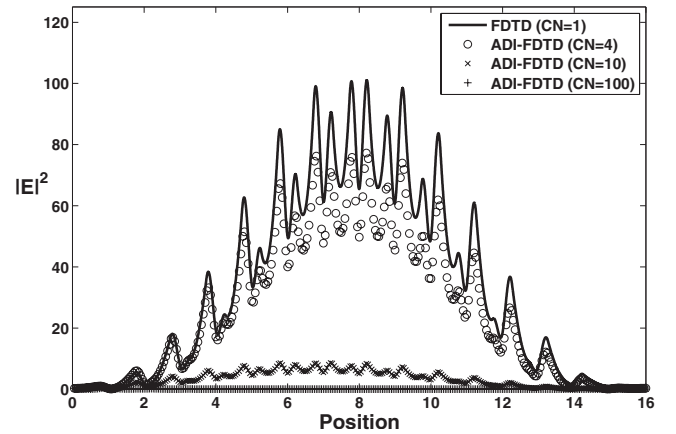

FIG. 18. ADI-FDTD results using various CNs for the steady-state time-averaged field intensity $|\mathbf{E}|^2$ inside the DBE PhC with $N=16$.

TABLE II. Comparison between FDTD, ADI-FDTD, and CE-ADI-FDTD results: DBE PhC with $N=16$.

Method	CN	$|\mathbf{E}|^2_{\max}$	CPU time
FDTD	1	201.9835	100%
ADI-FDTD	4	158.0580	102.59%
ADI-FDTD	10	25.6795	41.01%
ADI-FDTD	100	0.73460	5.67%
CE-ADI-FDTD	100	201.9235	13.01%
CE-ADI-FDTD	250	201.9235	5.25%
CE-ADI-FDTD	1000	200.5322	1.30%

$$- \gamma_{-,k}D^{n+1/2}_{y_{k-1}} + (1 + \beta_{-,k} + \beta_{+,k})D^{n+1/2}_{y_k} - \gamma_{+,k}D^{n+1/2}_{y_{k+1}}$$
$$= c_{d1,k}D^n_{y_k} + c_{d2,k}[c_{h1,k+1/2}H^{n+1/2}_{x_{k+1/2}} - c_{h1,k-1/2}H^{n+1/2}_{x_{k-1/2}}]$$
$$+ \gamma_{-,k}D^{n+1/2}_{x_{k-1}} - (\beta_{-,k} + \beta_{+,k})D^{n+1/2}_{x_k} + \gamma_{+,k}D^{n+1/2}_{x_{k+1}},$$
$$(A17)$$

where

$$\beta_{\pm,k} = c_{d2,k}c_{h2,k\pm1/2}c_{e1y,k},$$

$$\gamma_{\pm,k} = c_{d2,k}c_{h2,k\pm1/2}c_{e1y,k\pm1}. \qquad (A18)$$

For clarity, the spatial grid indexing is presented explicitly in the coefficients. The tridiagonal system can be efficiently solved in $O(N)$ operations. We can summarize the update procedure for the first substep as follows: (i) update $D^{n+1/2}_x$ explicitly from Eq. (A11), (ii) update $D^{n+1/2}_y$ implicitly from Eq. (A17), (iii) update explicitly $E^{n+1/2}_x$ from Eq. (A15) and $E^{n+1/2}_y$ from Eq. (A16), and (iv) update $H^{n+1/2}_x$ and $H^{n+1/2}_y$ explicitly from Eqs. (A13) and (A14), respectively.

An analogous procedure follows for the second substep. Note that the above algorithm recovers the conventional ADI-FDTD algorithm by setting the carrier frequency ω_c zero and by using real arithmetics. The above refers to lossless anisotropic dielectrics. The extension to lossy anisotropic dielectrics is presented in Ref. [28]

Figure 17 shows the steady-state time-averaged $|\mathbf{E}|^2$ inside the DBE PhC with $N=16$, calculated by the CE-ADI-FDTD and FDTD algorithms. Very good agreement is observed between FDTD and CE-ADI-FDTD results, for all CNs considered. On the other hand, a discrepancy is observed between ADI-FDTD and FDTD results, as shown in Fig. 18. The ADI-FDTD results start to be compromised for CNs as low as 4. The ADI-FDTD results deteriorate as the
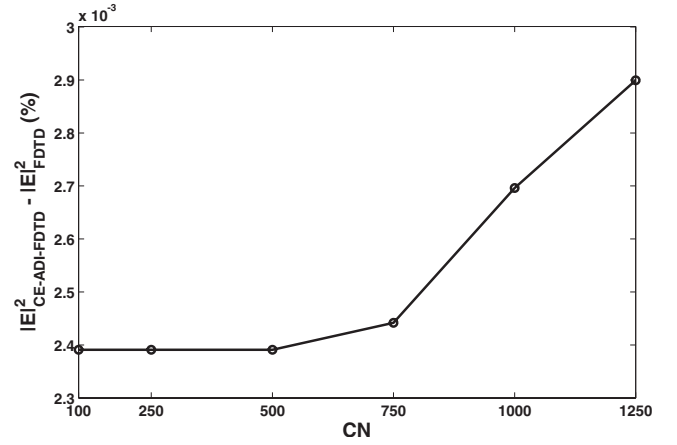

FIG. 19. Discrepancy between CE-ADI-FDTD and FDTD results for $|\mathbf{E}|^2$ inside the DBE PhC with $N=8$.

CN increases because of numerical dispersion.[18]

Table II summarizes the maximum value of the instantaneous field intensity ($|\mathbf{E}|^2_{\max}$) inside the DBE PhC and the normalized computation time for the three methods. We notice that the maximum value of instantaneous field intensity is twice as the maximum value of time-averaged field intensity. The difference of $|\mathbf{E}|^2_{\max}$ between the CE-ADI-FDTD algorithm with $N_C=250$ and the FDTD algorithm is only about 0.03%. For the same CN, the computation time of the CE-ADI-FDTD algorithm is longer than the ADI-FDTD algorithm because the former requires complex number arithmetic. Despite the increase of computation time for the same CN, the CE-ADI-FDTD algorithm reduces computation time dramatically because it allows for much larger time steps. For example, the CPU time of the CE-ADI-FDTD algorithm with $N_C=250$ is reduced to ca. 5.25% of the FDTD algorithm within 99.97% accuracy. In terms of memory requirements, the ADI-FDTD algorithm requires 27% more memory than the FDTD algorithm and the CE-ADI-FDTD algorithm requires 72% more memory than the FDTD algorithm, due mainly to complex arithmetic requirements.

Figure 19 shows the error in CE-ADI-FDTD results for various CNs in the case of the DBE PhC with $N=8$. The difference between the CE-ADI-FDTD and FDTD algorithms does not increase noticeably as the time step size is increased. In fact, the accuracy of the CE-ADI-FDTD results is nearly invariant unless $N_C \approx 750$ (as it approaches the Nyquist limit). Note that CE-ADI-FDTD algorithm has very small numerical dispersion error at the carrier frequency, as pointed out in Ref. [20].

[1] E. Yablonovitch, Phys. Rev. Lett. **58**, 2059 (1987).

[2] J. D. Joannopoulos, R. D. Meade, and J. N. Winn, *Photonic Crystals: Molding the Flow of Light* (Princeton University Press, Princeton, 1995).

[3] A. Figotin and I. Vitebsky, Phys. Rev. E **63**, 066609 (2001).

[4] A. Figotin and I. Vitebskiy, Phys. Rev. B **67**, 165210 (2003).

[5] A. Figotin and I. Vitebskiy, Phys. Rev. E **68**, 036609 (2003).

[6] A. Figotin and I. Vitebskiy, J. Magn. Magn. Mater. **300**, 117 (2006).

[7] A. Figotin and I. Vitebskiy, Waves Random Media **16**, 293

(2006).

[8] K.-Y. Jung, B. Donderici, and F. L. Teixeira, Phys. Rev. B **74**, 165207 (2006).

[9] R. A. Chilton, K.-Y. Jung, R. Lee, and F. L. Teixeira, IEEE Trans. Microwave Theory Tech. **55**, 2631 (2007).

[10] A. Figotin and I. Vitebskiy, Phys. Rev. E **72**, 036619 (2005).

[11] A. Taflove and S. C. Hagness, *Computational Electrodynamics: The Finite-Difference Time-Domain Method*, 2nd ed. (Artech House, Norwood, MA, 2000).

[12] H.-T. Chien, H.-T. Tang, C.-H. Kuo, C.-C. Chen, and Z. Ye, Phys. Rev. B **70**, 113101 (2004).

[13] A. Vial, A.-S. Grimault, D. Macias, D. Barchiesi, and M. L. de la Chapelle, Phys. Rev. B **71**, 085416 (2005).

[14] T. Namiki, IEEE Trans. Microwave Theory Tech. **47**, 2003 (1999).

[15] F. Zheng, Z. Chen, and J. Zhang, IEEE Microw. Guid. Wave Lett. **9**, 441 (1999).

[16] S. Wang and F. L. Teixeira, IEEE Microw. Wirel. Compon. Lett. **13**, 72 (2003).

[17] K.-Y. Jung and F. L. Teixeira, IEEE Photon. Technol. Lett. **19**, 586 (2007).

[18] S. G. Garcia, T. W. Lee, and S. C. Hagness, IEEE Antennas Wireless Propag. Lett. **1**, 31 (2002).

[19] H. Rao, R. Scarmozzino, and R. M. Osgood, Jr., IEEE Photon. Technol. Lett. **14**, 477 (2002).

[20] S. Ju, K.-Y. Jung, and H. Kim, IEEE Microw. Wirel. Compon. Lett. **13**, 414 (2003).

[21] C. Ma and Z. Chen, IEEE Trans. Antennas Propag. **53**, 971 (2005).

[22] O. Ramadan, IEEE Microw. Wirel. Compon. Lett. **17**, 4 (2007).

[23] A. V. Oppenheim and R. W. Schafer, *Discrete-Time Signal Processing* (Prentice-Hall, Englewood Cliffs, NJ, 1989).

[24] J.-P. Berenger, J. Comput. Phys. **114**, 185 (1994).

[25] W. C. Chew and W. H. Weedon, Microw. Opt. Technol. Lett. **7**, 599 (1994).

[26] F. L. Teixeira and W. C. Chew, IEEE Microw. Guid. Wave Lett. **7**, 371 (1997).

[27] F. L. Teixeira, K.-P. Hwang, J. Jin, and W. C. Chew, IEEE Trans. Antennas Propag. **49**, 902 (2001).

[28] K.-Y. Jung, F. L. Teixeira, and R. Lee, IEEE Antennas Wireless Propag. Lett. **6**, 643 (2007).